Published in "Journal of Materials Chemistry C 4(25): 5922–5931, 2016" which should be cited to refer to this work.

Ultrafast charge carrier dynamics in $CH_3NH_3PbI_3$: evidence for hot hole injection into spiro-OMeTAD†

Jan C. Brauer,*[a] Yong Hui Lee,[b] Mohammad Khaja Nazeeruddin[b] and Natalie Banerji[a]

Hybrid organic–inorganic metal perovskites have emerged as highly promising materials for solar energy conversion. However, key questions regarding the working principles of perovskite solar cells remain to be answered in order to improve the design of such devices. In the present study, we have investigated the influence of excess excitation energy on the initial photo-products generated from FTO/meso-TiO_2/$CH_3NH_3PbI_3$ samples. We find that upon resonant excitation at the band edge, part of the formation of free charges passes *via* an excitonic state that dissociates on the sub-picosecond time scale. An exciton binding energy of <10 meV is estimated from the lifetime of the exciton. On the other hand, if excess energy is available, free charges are directly generated. We have then investigated the hole injection into spiro-OMeTAD at the $CH_3NH_3PbI_3$/spiro-OMeTAD interface. By following spectroscopically the generation of the oxidized form of the molecular hole conductor spiro-OMeTAD, we confirm that the hole injection is essentially ultrafast and occurs on the sub-80 femtosecond time scale. On this time scale, the hole injection competes with carrier cooling after photo-excitation and therefore the charge injection can occur from non-thermalised states.

Introduction

In recent years, hybrid organic–inorganic perovskites have emerged as promising materials for highly efficient photovoltaic and photoelectrochemical devices, due to their impressive performance as light absorbers and charge transporters.[2–6] In addition to these applications, perovskite materials are now actively studied for integration into light emitting devices, such as diodes[7] or lasers,[8] and into field effect transistors.[9] Their advantage consists in a combination of properties usually found separately in inorganic or organic semiconductors: on the one side high charge carrier mobility, low exciton binding energy,[10,11] and long carrier diffusion length,[12,13] and on the other side easy processability, band gap tunability[12,14] and cost-effectiveness. Efforts made to improve the device architecture, material processing and design schemes have led to an increase of solar cell performance from 3.8%[15] to certified power conversion efficiencies exceeding 20%.[16] The nature and evolution of the initial photoexcited states, charge generation, charge transport and charge injection into hole- and electron-conductors have been studied experimentally by means of spectroscopy and theoretically,[4,10,17–21] but nevertheless a complete understanding of the initial and fundamental processes is still missing.

A thorough understanding of the processes following the photoexcitation of the relatively new perovskite materials is necessary for an appropriate design of the various interfaces present in the complete photovoltaic devices, in order to optimize the energy-level alignment, layer thickness and roughness as well as to balance the charge transport. For example, methylammonium lead iodide ($CH_3NH_3PbI_3$) has been used in different architectures for photovoltaic devices, including dye-sensitized solar cell configurations,[22] mesoscopic superstructures on Al_2O_3 scaffolds and planar heterojunctions.[23,24] Also, different perovskite deposition methods have been reported, starting either from solution[3] or from the vapour phase,[25] to improve the crystallinity and morphology. The composition of the perovskite phase has been varied by the introduction of mixed halides, mixed cations or mixed metal perovskites, to optimize the light absorption and charge transport properties.[14,20] It has been shown that the morphology of the perovskite material inside the mesoporous scaffold and in the compact capping layer has a significant impact on the device performance and on the spectral features.[18]

Although device designs without hole transporting materials (HTMs) have been shown to work well[26] and designs with ultrathin p-type transport layers have reached efficiencies $>16\%$,[11] the current record devices rely on HTMs such as spiro-OMeTAD.[27] The choice of the HTM and the nature of the HTM/perovskite interface are therefore of fundamental importance for the

[a] *Department of Chemistry, University of Fribourg, Chemin du Musée 9, CH-1700 Fribourg, Switzerland. E-mail: jan.brauer@unifr.ch*

[b] *Group for Molecular Engineering of Functional Materials, Institute of Chemical Sciences and Engineering, Ecole Polytechnique Fédérale de Lausanne, CH-1015 Lausanne, Switzerland*

† Electronic supplementary information (ESI) available: Additional information on the global analysis procedure as well as supplementary experimental data. See DOI: 10.1039/c6tc00763e

performance and stability of the photovoltaic devices.[28] Due to its good performance, spiro-OMeTAD serves as a benchmark for the development of new HTM materials. Therefore, the properties of spiro-OMeTAD and its working principles in perovskite solar cells need to be understood in depth in order to serve as a comparison to other HTM systems. Recently, we have shown that hole injection from photoexcited $CH_3NH_3PbI_3$ to polymeric HTMs, like poly-(triarylamine) (PTAA), or poly(3-hexylthiophene-2,5-diyl) (P3HT), occurs on the nanosecond timescale.[29] Previously, Piatkowski *et al.*[19] and Marchioro *et al.*[17] presented indications from femtosecond transient absorption (TA) spectroscopy that hole injection into spiro-OMeTAD is likely to be much faster, on the picosecond to sub-picosecond time scale. Ponseca *et al.* also suggested ultrafast, sub-picosecond hole injection from photoexcited $CH_3NH_3PbI_3$ to spiro-OMeTAD using time-resolved terahertz (THz) spectroscopy.[30] To the best of our knowledge, there exists however no direct evidence of the ultrafast generation of the oxidized state of spiro-OMeTAD, which would unambiguously confirm this. In the present study we have used femtosecond-resolved TA spectroscopy to interrogate the ultrafast initial photoinduced processes in FTO/meso-TiO_2/perovskite and FTO/meso-TiO_2/perovskite/spiro-OMeTAD samples at resonant excitation and excitation with excess energy. We directly monitor ultrafast hole injection into the HTM, occurring faster than carrier thermalisation.

Experimental methods

Sample preparation

A 200 nm-thick mesoporous-TiO_2 layer was formed on cleaned FTO glass substrates (Pilkington, TEC 15) by spin-coating a commercially available TiO_2 paste (Dyesol 30NRD). The substrates were baked at 500 °C for 30 min, and cooled down to room temperature before deposition of the perovskite layer by the two-step deposition method.[3] For the deposition of the perovskite layer, 0.6 M PbI_2 solution in DMF was spin-coated on the substrate at 6500 rpm for 20 s. The film was dried at 90 °C for 15 min and then cooled down to room temperature. Consequently, the film was dipped into methylammonium iodide (MAI) solution (8 mg of MAI in 1 mL of isopropanol (IPA)) for 15 s, rinsed with IPA and dried at 70 °C for 5 min. For the deposition of the HTM, spiro-OMeTAD (Merck) solution was spin-coated on the perovskite film at 3000 rpm for 30 s while the thicker layer was prepared at 1500 rpm for 2 min. The spiro-OMeTAD solution was made by dissolving 72.3 mg of spiro-OMeTAD, 28.8 μL of 4-*tert*-butylpyridine (TBP, Aldrich), 17.5 μL of a stock solution of 520 mg mL^{-1} of lithium bis(trifluoromethylsulphonyl)imide in acetonitrile in 1 mL of chlorobenzene. All the preparative work and deposition of PbI_2, perovskites and HTMs were done inside a drybox to minimize the influence of moisture. An absorption spectrum as well as SEM images are presented in Fig. 1(A) and (B) respectively.

Transient absorption spectroscopy

Transient absorption (TA) spectra were recorded using femtosecond pulsed pump–probe spectroscopy. The measurements were performed in a sealed chamber under nitrogen to prevent degradation by oxygen and humidity. The probe beam consisted of a white light continuum (400–1200 nm), generated by passing part of the 800 nm amplified 1 kHz Ti:sapphire output (Coherent, Astrella) through a 5 mm sapphire plate. The remaining intensity of the fundamental was removed by a 750 nm low pass filter. Excitation pulses at 580 nm or 760 nm were generated in an OPA (OperaSolo, Coherent). To avoid any excitation-intensity effects,

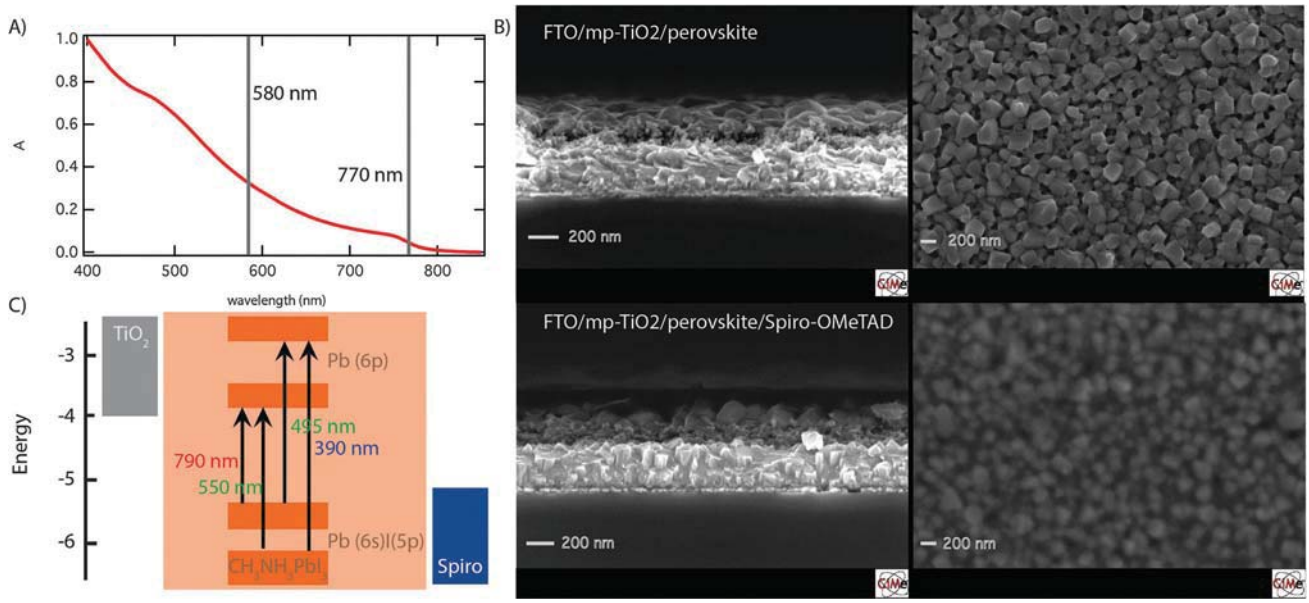

Fig. 1 (A) Absorption spectrum of a FTO/meso-TiO_2/$CH_3NH_3PbI_3$ sample. The lines indicate the excitation wavelengths for the femtosecond transient absorption experiments. (B) SEM pictures of FTO/meso-TiO_2/$CH_3NH_3PbI_3$ and FTO/mp-TiO_2/$CH_3NH_3PbI_3$/spiro-OMeTAD samples. (C) Simplified band alignment diagram for meso-TiO_2/$CH_3NH_3PbI_3$/spiro-OMeTAD samples, where transition energies are adopted from Zhu *et al.*[1]

the data presented in the following were recorded at low fluence (<2.5 μJ cm^{-2} and <6.5 μJ cm^{-2} for 580 nm and 760/770 nm excitation respectively). Fluence dependent measurements are shown in the ESI.† The probe intensity was always less than the pump intensity, and the probe spot size was chosen to be much smaller than the pump spot size to allow for a homogeneous excitation over the probed area. The pump/probe pulses were delayed with respect to each other using a computerized translation stage.

The probe pulses were split before the sample by means of a beamsplitter into a signal (transmitted through the sample and crossed with the pump) and a reference beam. The probe signal and reference beams were then detected separately using a pair of spectrographs (home-built prism spectrometers), equipped with 512 × 58 pixel back-thinned CCDs (Hamamatsu S07030-0906) and assembled by Entwicklungsbüro Stresing, Berlin. The pump beam was chopped as half the amplifier frequency to improve the sensitivity of the set-up. The transmitted intensity of the probe beam was recorded shot by shot and corrected for laser intensity fluctuations using the reference beam. The transient spectra were averaged at each delay until the desired signal-to-noise ratio was achieved. To avoid polarization effects, the relative polarization of the probe and pump pulses was set to the magic angle. All spectra were corrected for the chirp of the white-light probe.

In the global analysis procedure, the dynamics at all wavelengths were analysed simultaneously by a convolution of a Gaussian instrument response function (IRF, shown in the ESI†) and the sum of 2 or 3 exponentials. The amplitudes were allowed to vary freely for each wavelength, while the time constants were set to be the same for the whole spectral range. Plotting the amplitudes resulting from the fit against the wavelength yielded decay associated spectra, which indicate the features of the TA spectrum evolving with the same time constant. More details of the global analysis can be found in the ESI.†

Results and discussion

Absorption spectra and the band structure

$CH_3NH_3PbI_3$ shows broad-band light absorption spanning the whole visible spectrum, making it particularly suitable as an absorber in photovoltaic devices. Fig. 1(A) shows a typical absorption spectrum of a FTO/meso-TiO_2/$CH_3NH_3PbI_3$ sample, which is dominated by the transitions in the perovskite. At room temperature, the absorption spectrum of $CH_3NH_3PbI_3$ shows two peaks at about 790 nm and 490 nm. The lower energy transition, at 790 nm, is the direct band gap transition from the valence band (VB) to the conduction band (CB). The assignment of the higher energy transition is less clear. In recent theoretical studies, the band-structure of the perovskite has been investigated for different crystalline phases and compositions.[20,31] At room temperature, $CH_3NH_3PbI_3$ is in its tetragonal phase and the VB is mainly composed of Pb(6s) and I(5p) orbitals, while the CB mainly consists of Pb(6p) orbitals. The organic cation supposingly interacts only slightly with the inorganic PbI_6 octahedra, but it was shown that under certain conditions, molecular alignment of the organic cations might lead to a shift of the CB minimum leading to an indirect transition.[32] The broad and strong absorption of the perovskite is attributed to the multiband gap and multivalley nature of the material. Even *et al.* have predicted the ground-state optical transition at 790 nm, at the *R* point between doubly degenerate $E_{1/2g}$ VBM states and $E_{1/2u}$ CBM states. Furthermore, they have suggested higher energy transitions at the *R* point with energies of about 400 nm and 560 nm, $E_{1/2,g} \rightarrow F_{3/2,u}$ and $F_{3/2,g} \rightarrow E_{1/2,u}$ respectively, and at the *M* point with an energy of about 460 nm. They conclude that the absorption peak at 490 nm originates from a superposition of the above-mentioned transitions, mainly from transitions at the *M* point followed by carrier redistribution *via* a channel from *R* to *M*.[33–35] Zhu *et al.* predicted as well several transitions in the visible range and two accessible conduction and valence bands, the corresponding transition energies are given in Fig. 1(C).[1] Experimentally, the existence of multiple valence and conduction bands has been invoked to explain TA data. Xing *et al.* proposed a model of two VBs and one CB to explain the observed change in the ground state bleaching recovery dynamics when the perovskite layer is in contact with an electron or a hole acceptor.[36] Marchioro *et al.* on the other hand proposed a system of two CBs and two VBs to explain their spectroscopic results.[37] Very recently, Sum *et al.* pointed out the sensitivity of the measured charge carrier dynamics on the sample preparation as well on the measurement conditions. Their findings support the dual conduction band picture, in agreement with Marchioro *et al.*[38]

Excitation wavelength dependence

In the first part of this study, we have investigated the excitation wavelength dependence by exciting a FTO/meso-TiO_2/$CH_3NH_3PbI_3$ film at the band-edge (770 nm) and in-between the band-edge and the second, higher-energy transition (580 nm). At the longer wavelength we excite the perovskite just at the lowest electronic transition as discussed in the previous paragraph without populating thermally excited states in the conduction band. Exciting at 580 nm will lead to thermally excited carriers and only minor excitation of the electronic transitions at higher energies, which are supposed to be at 560 nm and shorter wavelengths.

Fig. 2 shows the TA spectra and time profiles of the FTO/meso-TiO_2/$CH_3NH_3PbI_3$ sample upon photoexcitation at 580 nm. Two prominent negative signals are seen at ~500 nm and 750 nm, as well as a broad photoinduced absorption at 530–730 nm. The positive band contains information about the excited population, about hot states at early times and thermally relaxed charges at later times.[19] Recently Price *et al.* reported that the positive signal is related to a photoinduced reflectivity change due to a refractive index change induced by free charges and not to a transient absorption feature.[39] Yang *et al.* reproduced the spectral shape of the low energy bleach and positive signal by considering contributions from free carriers as well as excitonic states.[40] The negative bands have been previously described as bleaching of the transitions from two VBs to a common CB.[36] Alternatively, the existence of a dual excited state composed of a charge transfer band at 480 nm and a lower energy band-edge has been proposed.[41]

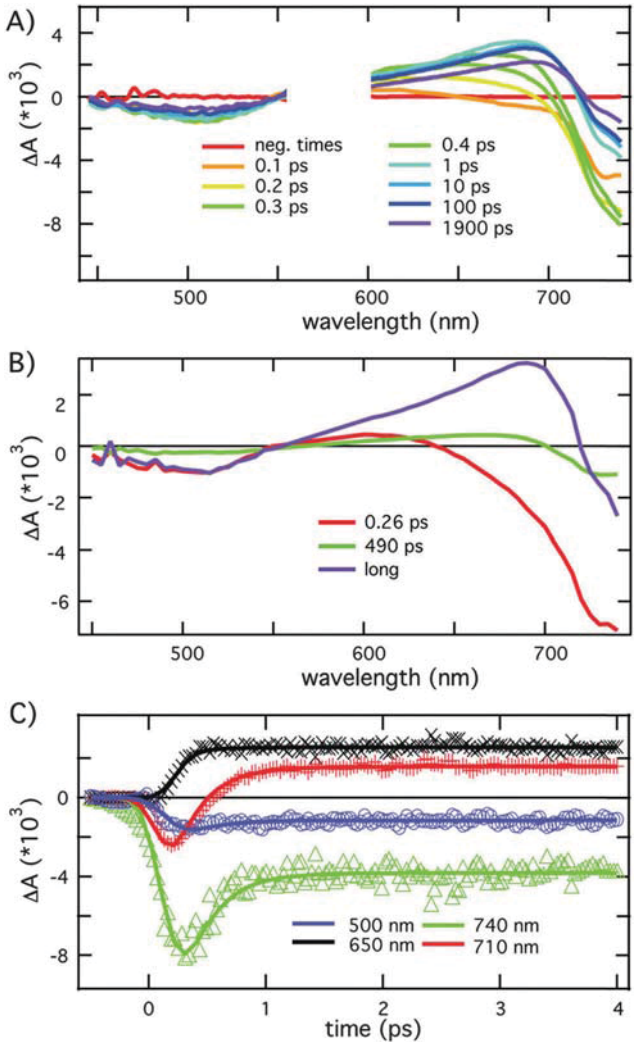

Fig. 2 (A) Transient absorption spectra following 580 nm excitation of a FTO/meso-TiO_2/$CH_3NH_3PbI_3$ film. (B) Decay-associated spectra obtained by global analysis (with the sum of exponential terms convoluted with the Gaussian IRF) of the dynamics related to (A). (C) Selected time traces from the TA data of the FTO/meso-TiO_2/$CH_3NH_3PbI_3$ sample following 580 nm excitation. Solid lines show the best fit resulting from the global analysis of the time traces.

Flender *et al.* measured TA spectra of PbI_2 on TiO_2 and showed that bleaching at 500 nm is not related to plumbate, possibly remaining in the perovskite samples.[42] We also cannot exclude a contribution of stimulated emission to the negative signal around 750 nm. In Fig. 2, we observe a sub-picosecond spectral narrowing on the blue side of the 750 nm band upon excitation at 580 nm, together with a rise of the overlapping positive band. This has been explained by band filling effects or by stimulated emission from thermally non-relaxed states.[43] At the low excitation density (2.5 μJ cm^{-2}) used in our experiments, we expect the observed sub-picosecond component to be mainly related to emission from thermally non-relaxed states. This interpretation also correlates with the recovery of the bleaching transition at ~500 nm occurring at the same time scale as the emission from non-thermalised states of approximately 250 fs. The fast relaxation is reflected in the decay-associated spectrum with a 0.26 ps time constant, and is seen in the early time traces (Fig. 2B and C). In the dynamics (Fig. 2C) the emission from non-thermalised states and the corresponding ground-state recovery can be seen as sub-ps dynamics at 740 nm, 710 nm and 500 nm. The latter shows the ground-state recovery that increases the probability for higher energy transitions at the *R* point with energies of about 400 nm and 560 nm, $E_{1/2,g} \rightarrow F_{3/2,u}$ and $F_{3/2,g} \rightarrow E_{1/2,u}$ respectively, and at the *M* point with an energy of about 460 nm as discussed previously.

In the FTO/meso-TiO_2/$CH_3NH_3PbI_3$ sample, there is supposedly electron injection from the photoexcited perovskite to TiO_2. This has been reported to be ultrafast and should therefore occur in our experiments. Ponseca *et al.* have investigated electron injection by optical-pump–THz-probe spectroscopy and compared the signal of perovskites on TiO_2 and Al_2O_3 scaffolds.[44] They observed, upon excitation at 400 nm, a prompt reduction of the signal amplitude to about one-third in the case of TiO_2 (faster than their experimental time resolution of approximately 1 ps), attributed to ultrafast electron injection into TiO_2, energetically not feasible with Al_2O_3. They also saw the decay of a 2 ps component, attributed to exciton splitting in Al_2O_3/perovskite and neat perovskite films. Marchioro *et al.* investigated charge injection from photoexcited $CH_3NH_3PbI_3$ by means of NIR pump–probe spectroscopy and also found that part of the electron population should be injected into TiO_2 on a time scale of <3 ps.[17] Piatkowski *et al.* estimated the electron injection dynamics based on the PIA feature at 870 nm to occur within 200 fs.[19] In the probed wavelength range electron injection into TiO_2 should manifest itself by a decrease of the signal related to free charge carriers in perovskites. We have observed reduced amplitude, at early times when exciting at short wavelength, <500 nm, and are currently investigating this effect in depth. This observation is in agreement with Xing *et al.* who observed hot electron injection into TiO_2.[45]

Fig. 3 shows the TA spectra of the FTO/meso-TiO_2/$CH_3NH_3PbI_3$ film upon excitation at 770 nm. Exciting at 770 nm results in a transition without excess energy, just at the band-edge. In the TA spectra, we still observe the negative signals at ~500 nm and above 720 nm, as well as the positive signature from 550 nm to ~720 nm. Since, with excitation at 770 nm, there is no excess energy, we do not observe the fast sub-picosecond relaxation involving the broadened stimulated emission from thermally non-relaxed states at early times that are present upon excitation at 580 nm. However, we observe a blue shift and broadening of the positive TA signature. At early times, there is a maximum at about 710 nm and shifts within 0.2 ps to 690 nm. This feature is as well clearly observable in the decay-associated spectrum shown in Fig. 3(B). While the long-lived component is similar to the long-lived component observed upon 580 nm excitation, the 0.2 ps component is fundamentally different and shows now a positive feature peaking at >720 nm. The short-lived (0.26 ps) negative feature in the decay associated spectrum upon 580 nm excitation describes the decay of a bleaching or fluorescence, on the other hand the positive feature in the decay associated spectrum upon 770 nm excitation describes the decay of a

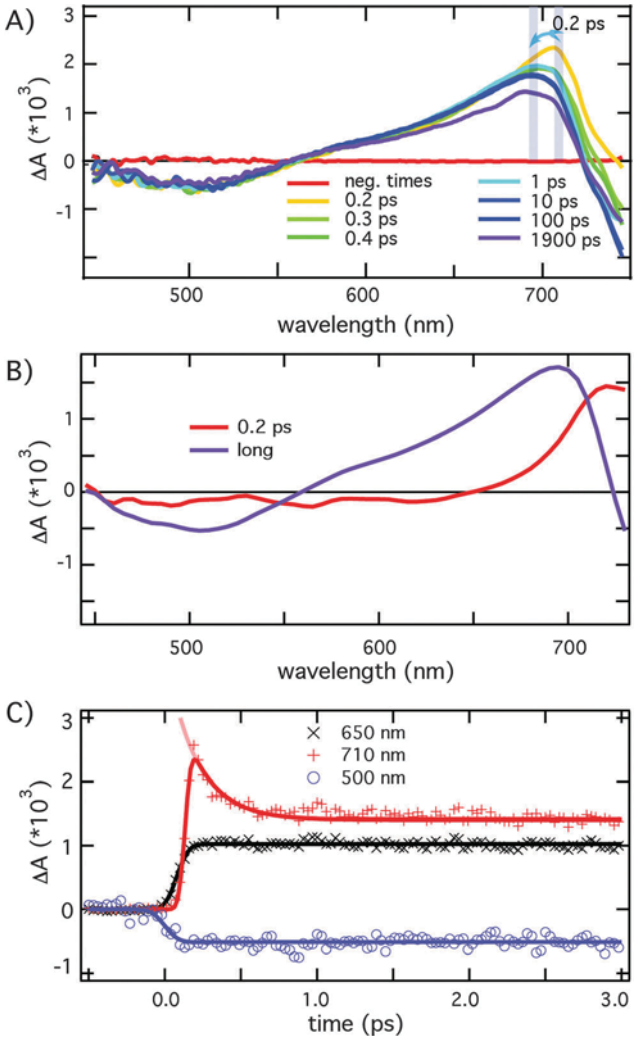

Fig. 3 (A) Transient absorption spectra following 770 nm excitation of a FTO/meso-TiO_2/$CH_3NH_3PbI_3$ film. (B) Decay-associated spectra obtained by global analysis (with the sum of exponential terms convoluted with the Gaussian IRF) of the dynamics related to (A). (C) Selected time traces of the FTO/meso-TiO_2/$CH_3NH_3PbI_3$ sample following 770 nm excitation. Solid lines show the best fit resulting from the global analysis (convolution of a Gaussian with two exponential functions). The semi-transparent solid red line shows the analysis with a double exponential function not convoluted with the Gaussian IRF.

photo-induced absorption peak. Grancini *et al.* investigated the influence of the crystallite size on the formation of excitons in perovskites.[18] They observed the formation of long-lived $CH_3NH_3PbI_3$ excitons (indicated by a photo-induced absorption at ~740 nm) in the capping layer of meso-Al_2O_3/$CH_3NH_3PbI_3$ samples at 170 K, and in 'cuboids-like' $CH_3NH_3PbI_3$ films with a controlled crystal size of ~1 μm at RT upon excitation at ~520 nm. In accordance with their spectral assignment, we can attribute the short-lived TA feature at >720 nm to the formation of excitons upon resonant band-gap excitation. Our samples show a crystallite size of approximately 200 nm in the capping layer (Fig. 1B) and much smaller grain size within the mesoporous structure. Therefore, we see, in accordance with Grancini *et al.*, no long-lived excitons, but a rapid splitting of the excitons into free charges. The dynamic of the exciton splitting is reflected by the sub-ps dynamics probed at 710 nm, Fig. 3(C).

The binding energy of excitons in $CH_3NH_3PbI_3$ is reported to be low in the range of 2–55 meV,[10,11,33] suggesting that photo-excitation leads primarily to the generation of free charge carriers. Ultrafast spectroscopy studies have been previously performed to identify the nature of the initial excitation products[18,46] it has been shown that the grain size has an important impact on the initial photo-products.[18] The excitonic binding energy in $CH_3NH_3PbI_3$ is also related to the disorder in polycrystalline systems. Larger crystals have been shown to have a higher degree of order due to the presence of a cooperative ordered phase of the organic cation.[21] Therefore a higher degree of disorder is expected within the smaller crystallites in the mesoporous phase[47] going along with a reduced exciton binding energy. The exciton binding energy is crucial for the understanding of the functioning of solar cells, since it defines the fraction of carriers that are present as free or bound charges. Values of the exciton binding energy of $CH_3NH_3PbI_3$ presented in the literature range from 2 to 55 meV.[10,11,34,48,49] This low binding energy suggests that at room temperature, charge-carriers are predominantly present as free charges and that excitons only represent a minor part of the excited-state population. Assuming that, when exciting at 770 nm, part of the initial photoexcited population is of excitonic nature (as suggested by the >710 nm peak), the rate of the observed frequency shift at >710 nm allows us to roughly estimate the binding energy of the excitons based on the Eyring equation, that relates the rate of a process to its activation energy. A time constant of 0.2 ps relates to a binding energy of ~6 meV, which is in very close agreement with previous reports of the exciton binding energy in $CH_3NH_3PbI_3$ and supports the assignment of the peak at ~710 nm to the initially formed excitons. Thus, exciting above the band gap at 580 nm leads to the direct generation free charges, while exciting at 770 nm leads to a short-lived transient population of excitons prior to ultra-fast splitting of the charge pairs. This allows the conclusion that the broad positive signature, observed at later times (>2 ps) with a maximum at 690 nm, which has been attributed to the absorption of charges and excitons,[19] or to a reflectivity modification due to a change in the refractive index induced by the free-carrier population,[39] is indeed a signature of free charges in agreement with the latter.

The lifetime of the free carriers in the perovskite largely exceeds our measurement window of 1.9 ns, so that we see only the onset of a decay (Fig. 2A and 3A). The long radiative lifetime of perovskites (>250 ns)[13,50] suggests a low defect density in perovskite films, which is surprising for solution-processed semiconductors. Trap densities have been determined to be as low as ~10^{-10} cm^{-3} in single crystals[51] and considerably higher in polycrystaline films (10^{15}–10^{16} cm^{-3}).[52–54] deQuilletes *et al.* measured spatially resolved photoluminescence decay dynamics and found that even films with very long radiative lifetimes show substantial local heterogeneity, entire dark grains and grain boundaries with reduced photoluminescence efficiency, lifetime and the shifted emission spectrum being indicative of defects and shallow traps.

Hole injection into spiro-OMeTAD

In order to study hole injection from photoexcited $CH_3NH_3PbI_3$ to the molecular hole-conductor spiro-OMeTAD, we have recorded the TA spectra of a FTO/meso-TiO_2/$CH_3NH_3PbI_3$/spiro-OMeTAD sample, following excitation at 580 nm and 760 nm. This hole injection has been investigated by several groups using different time-resolved spectroscopic techniques.[17,19,22,36,37] The quenching of the perovskite photoinduced absorption or of its fluorescence in the presence of spiro-OMeTAD has been observed, but to the best of our knowledge, direct spectral evidence of the ultrafast generation of the oxidized form of spiro-OMeTAD has not been reported yet. When investigating samples prepared from solution using the typical procedure for solar cell fabrication (see Experimental methods), we observe a reduction of the amplitudes of the features related to photoexcited perovskites in the presence of spiro-OMeTAD layers, compared to samples without HTM. TA spectra and dynamics at 690 nm are presented in Fig. 4, in the presence and absence of HTM. It can be seen that the initial amplitude of the positive band is reduced already at very early times when spiro-OMeTAD is added, in agreement with the literature.[22,37] The dynamics at 690 nm upon excitation at 580 and 760 nm reflect the evolution of the free carrier population in the perovskite as discussed in the previous paragraph. In the case of 580 nm excitation we first see a short lived negative signal at a probe wavelength of 690 nm (Fig. 4B) due to emission from non-thermalised states. At longer times the signal is positive and decays slowly after an initial ingrowth. The dynamics do not change substantially upon addition of spiro-OMeTAD but the amplitude is reduced. Upon excitation at 760 nm, we do not see the emission at early times but we see a fast decrease of the positive signal in the first picosecond. This decrease is related, as described in the previous paragraph, to the exciton splitting. The fast decrease is followed by a long-lived signal. As in the case of 580 nm excitation, we do not see a difference in the dynamics upon addition of spiro-OMeTAD but a decrease of the signal amplitude by about 30%. The amplitude reduction and the fact that the time evolution of the dynamics is very similar with and without the HTM suggest that the hole injection occurs already at ultrafast times. This alone is nevertheless not an unambiguous proof of hole injection, since Price *et al.* discovered that the signal at this wavelength is due to a photo-induced reflectivity change.[39] Adding a supplementary organic layer changes the refractive index contrast and therefore the reflectivity of the sample. Also, the spatially resolved photoluminescence decay dynamics reported by deQuiletes *et al.* show that treatment with pyridine leads to a substantial reduction of the trap density and increase of the PL brightness.[55] This suggests that contacting a perovskite film with either an electron or a hole accepting layer might act on the dynamics measured by transient techniques not only by facilitating charge injection, but by possibly changing the trap density of the film. For these reasons, only direct observation of oxidized spiro-OMeTAD presents an un-ambiguous signature for hole injection dynamics.

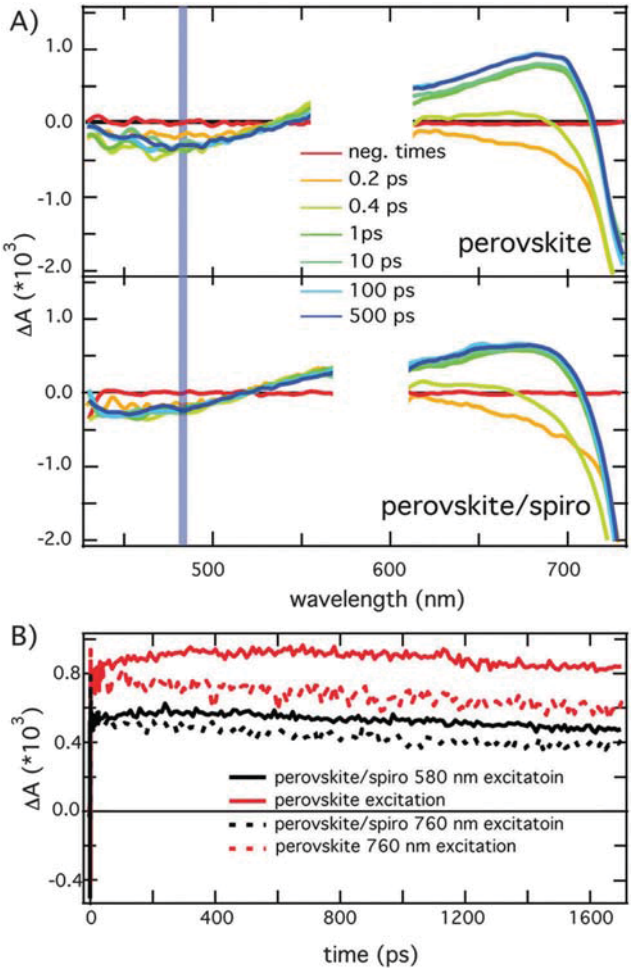

Fig. 4 (A) Transient absorption spectra upon 580 nm excitation of FTO/meso-TiO_2/$CH_3NH_3PbI_3$ and FTO/meso-TiO_2/$CH_3NH_3PbI_3$/spiro-OMeTAD films (B). Time traces recorded at 690 nm upon excitation at 580 nm and 760 nm of the FTO/meso-TiO_2/$CH_3NH_3PbI_3$ and FTO/meso-TiO_2/$CH_3NH_3PbI_3$/spiro-OMeTAD samples.

A closer inspection of the bleaching band at ~500 nm (Fig. 4A) reveals a small blue shift in the presence of spiro-OMeTAD, even at very early times. The shift is also observed when exciting the sample at 760 nm (see ESI,† Fig. S6). It could be due to the overlap of the positive absorption signal due to oxidized spiro-OMeTAD, with the ground state bleaching of neutral spiro-OMeTAD and the bleaching band of the perovskite. The steady-state spectrum of neutral spiro-OMeTAD shows absorption bands at ~300 nm and from 330 nm to 420 nm. Oxidizing spiro-OMeTAD leads to an ingrowth of bands at 430–550 nm and at ~650–750 nm, as well as to further peaks in the NIR range.[56,57] Therefore, it is likely that the observed shift of the 500 nm signal in the TA data is related to the formation of the oxidized form of spiro-OMeTAD.

To investigate this further, we have enhanced the spectral signature of the oxidized form of the HTM by increasing the thickness of the spiro-OMeTAD layer. Transient spectra and selected time traces of this film in comparison to a film deprived of the spiro-OMeTAD layer are presented in Fig. 5. Here, it is even more evident that the negative signal around 500 nm is blue-shifted and spectrally wider in the presence of the HTM, and that the amplitude in the 550 to 700 nm range is substantially

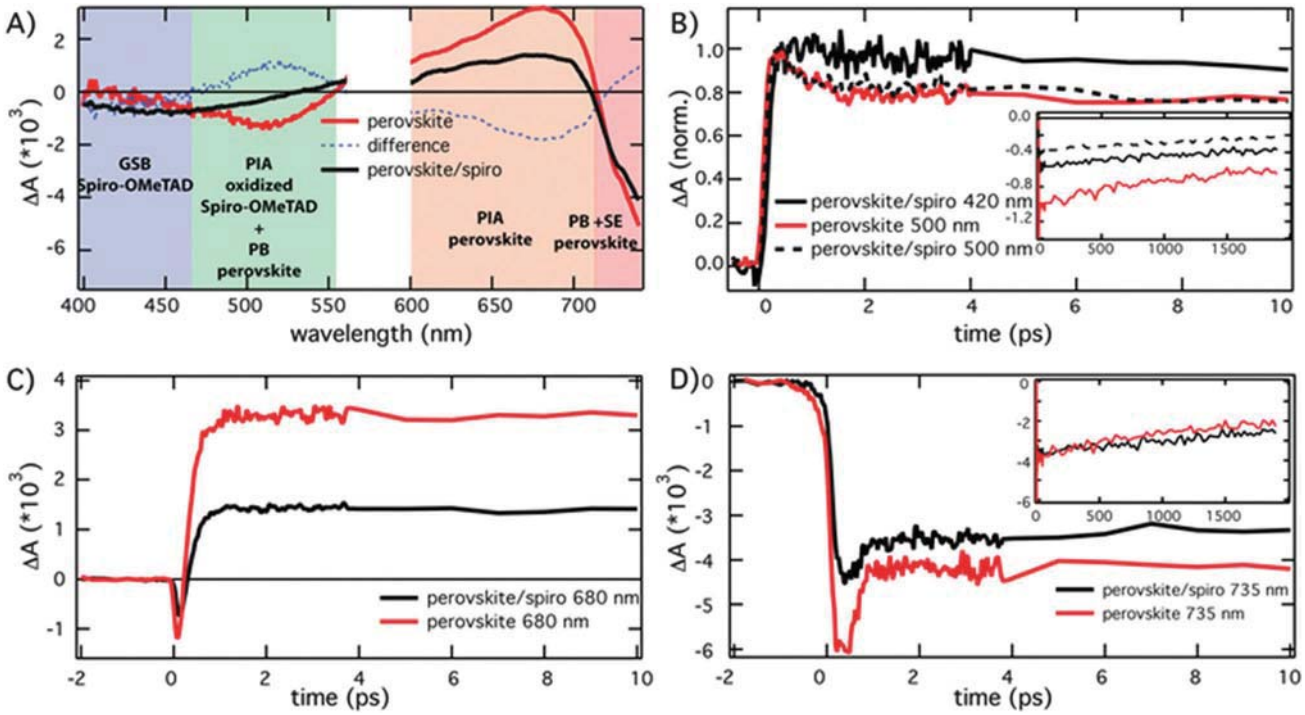

Fig. 5 (A) Transient absorption spectra of FTO/meso-TiO_2/$CH_3NH_3PbI_3$, FTO/meso-TiO_2/$CH_3NH_3PbI_3$/spiro-OMeTAD (high HTM loading) and the corresponding difference spectrum, 1 ps after excitation at 580 nm. (B) Corresponding time traces recorded at 420 nm and 500 nm (the inset shows the non-normalized data on a longer time scale). (C) Comparison of the dynamics recorded at 680 nm with and without the HTM. (D) Comparison of the dynamics at 735 nm with and without the HTM (the inset shows the non-normalized data on a longer time scale).

decreased. The difference of the spectra of the FTO/meso-TiO_2/$CH_3NH_3PbI_3$ film and the FTO/meso-TiO_2/$CH_3NH_3PbI_3$/spiro-OMeTAD film (with thick HTM layer) was taken at 1 ps after photoexcitation to subtract the features related to the excited perovskites (Fig. 5A). This clearly reveals a bleaching band in the 400–430 nm region and a photoinduced absorption band in the 460–560 nm region. These peak positions coincide very well with the expected ground-state bleaching of spiro-OMeTAD and the absorption of the oxidized spiro-OMeTAD generated by hole injection from the photoexcited perovskite.[56,57] The negative feature of the difference spectrum in the 600–720 nm region as well as the positive feature at longer wavelengths mirror the shape of the photoexcited perovskite and the results from the decreased excited state and free charge carrier population in $CH_3NH_3PbI_3$, due to hole injection into the HTM. Having identified the absorption and bleaching contributions of the oxidized spiro-OMeTAD, as well as knowing the spectral features of photoexcited $CH_3NH_3PbI_3$, we can isolate a spectral region that almost exclusively monitors the hole injection: below 450 nm, the contribution of photoexcited $CH_3NH_3PbI_3$ is negligible and the negative TA band reflects essentially the bleaching of spiro-OMeTAD. Therefore, following the dynamics at $\sim$420 nm allows us to directly monitor the population of oxidized spiro-OMeTAD and consequently the hole injection. The corresponding normalized time trace is shown in Fig. 5(B). A response-limited rise time indicates that the hole injection occurs on a sub-80 fs time scale. For comparison, the dynamics for the TiO_2/$CH_3NH_3PbI_3$ and TiO_2/$CH_3NH_3PbI_3$/spiro-OMeTAD sample at 500 nm (mainly the bleaching signal from $CH_3NH_3PbI_3$ and some absorption of oxidized spiro-OMeTAD) are shown. At this wavelength, similar dynamics are dominated by carrier cooling in the perovskite. The different dynamics at early times observed for the FTO/meso-TiO_2/$CH_3NH_3PbI_3$/spiro-OMeTAD sample at 420 nm and 500 nm clearly confirm that different photoproducts are probed. This supports the choice of 420 nm as wavelength to probe the hole injection from photo-exited perovskite to spiro-OMeTAD.

TA time profiles probed at 680 nm and 735 nm are shown in Fig. 5(C) and (D). The positive signature of the perovskite at 680 nm is almost reduced to half its amplitude in the presence of the HTM, but as mentioned previously, this might not be a proof of a substantial reduction of free charge carriers, due to the contribution of transient reflectivity. We note nevertheless that even the early stimulated emission from thermally non-relaxed carriers, manifested by the short-lived (sub-picosecond) negative feature at 680 nm (Fig. 5(C)), is reduced in the presence of spiro-OMeTAD. This reduction of the stimulated emission gives a more direct access to the population of electrons and holes in the perovskite layer. The stimulated emission from non-thermalised states occurs on a sub-ps time scale (τ = 0.26 ps, Fig. 2(B)). The reduction of this stimulated emission indicates that hole injection into spiro-OMeTAD competes with thermalisation and that it can occur from hot states. Similarly, Xing *et al.* observed that efficient electron injection at a perovskite/TiO_2 interface occurs from hot, non-thermalised states due to an interfacial energy barrier.[45] This shows that due to the relatively slow thermalisation of hot carriers to the band edge, charge

injection from non-thermalised states can occur at the hole- and electron extracting interface and should be considered when designing the band alignment.

The negative TA band at >710 nm is less quenched in the presence of the HTM than the signals at lower wavelengths (Fig. 5A). This can be explained as follows: the signal at >710 nm is due to stimulated emission from the band edge as well as due to a depletion of the band-edge transition (bleaching). The depletion of the band-edge transition occurs after hole injection, due to the remaining carrier concentration in the conduction band. By comparing the two time-traces in Fig. 5(D), recorded at a probe wavelength of 735 nm, we find that the sub-picosecond component of the dynamics is strongly quenched by the presence of spiro-OMeTAD, while the amplitude of the slow component is relatively less affected. The fast component, being due to stimulated emission from non-thermalised states, requires both the electron and hole to be present in the conduction and valence band of the perovskite, respectively. This emission is quenched due to the fast hole injection into spiro-OMeTAD from the perovskite valence band. The bleaching results from a depletion of the valence band population and an increase of the conduction band population, rendering the band-gap transition less probable. The hole injection into the HTM leads to an increase of the valence band electron population, but the electrons left behind in the conduction band cause a persistent bleaching on the investigated time scale. Only on a longer time scale (inset of Fig. 5D), we observe that the dynamics of the ground state recovery is delayed in the case of the $TiO_2/CH_3NH_3PbI_3$/spiro-OMeTAD sample due to the charge separation across the $CH_3NH_3PbI_3$/spiro-OMeTAD interface.

We have observed ultrafast hole injection to spiro-OMeTAD when exciting the perovskite at 580 nm and 760 nm. Therefore, we can conclude that no excess energy is necessary for ultrafast hole injection. We also found that upon resonant excitation, excitons are generated that split on a time scale of 200 fs, which is slower than the injection into spiro-OMeTAD. To resolve this contradiction, we reason that even upon excitation resonant with the band-gap, only part of the excited population will form excitons while the other part will form directly free charges. The ultrafast hole injection occurs most likely from the free charges. This is reasonable, since within the mesoporous layer and the capping layer, we find a distribution of crystallite dimensions with an upper limit of approximately 200 nm (Fig. 1(B)). The exciton binding energy in the smaller crystals is supposed to be largely inferior to the estimated <10 meV, so that hole injection from these crystallites to spiro-OMeTAD can be ultrafast.

In a recent study, we have investigated the hole injection from photoexcited perovskites to polymeric HTMs including PTAA and P3HT.[29] We found that the hole injection in the case of polymeric HTMs occurs on a time scale of a few nanoseconds. Comparing this to the ultrafast injection in the case of spiro-OMeTAD is astonishing from the thermodynamical point of view. The oxidation potentials for P3HT, PTAA and spiro-OMeTAD are -5.1 eV, -5.2 eV and -5.22 eV, respectively, suggesting a similar driving force for hole injection in the three compounds. In the case of the polymers, scanning electron microscopy (SEM) suggested some areas with poor physical contact. In contrast, the contact at the spiro-OMeTAD/perovskite interface is much better. Moreover, we cannot exclude that the ultrafast hole injection stems from an unusual good coupling of the triphenyl-group of the spiro-OMeTAD to the perovskite. To ensure good coupling, the lowest unoccupied molecular orbital (LUMO) of the HTM molecules has to be in close proximity and in the right orientation with respect to the perovskite lattice. Spiro-OMeTAD can interact *via* the oxygen-containing groups with the perovskite, which improves the electronic coupling. Comparing this work with our previous work suggests that engineering of HTMs should focus mainly on small molecule HTMs, containing the right side-groups, to ensure a better physical and electronic contact of the HTM with the perovskite. The first reasoning is thought to be more important in the case of non-planar perovskite surfaces, while the second should be of general validity.

Conclusions

We have shown that upon resonant excitation, excitonic states are in part initially populated in the $CH_3NH_3PbI_3$ perovskite. The photogenerated excitons dissociate on a time scale of a few hundred femtoseconds into free charges. From the dissociation time, we have estimated the exciton binding energy to be <10 meV, which closely compares to previous estimations by different techniques. Upon photoexcitation with excess energy, we do not see the spectral signature of the excitonic states and conclude that free charges are directly formed. In this case, the cooling of the hot carriers was monitored and we find that it occurs on a sub-picosecond time scale. These results indicate that, for the investigated samples, free charges are generated within one picosecond, no matter if excess energy is provided or not. Hole injection from photoexcited perovskite to spiro-OMeTAD has then been investigated. A probe wavelength in the transient absorption spectra was identified, which allows for the first time to directly follow the population of oxidized spiro-OMeTAD. We have shown that the hole injection from free charges occurs on a sub-80 fs time scale, independently of the excitation energy. However, in the presence of excess energy, there is evidence of hot hole injection. This opens up the opportunity to design perovskite/HTM interfaces with lower thermodynamic driving force and higher V_{oc} in devices.

Acknowledgements

The authors thank Jingshuan Luo (EPFL) for taking the SEM images. N. B. and J. C. B. thank the Swiss National Science Foundation (PP00P2_15036) and the University of Fribourg for funding, as well as Prof. J.-E. Moser (EPFL) and Dr A. Marchioro for useful discussions. Y. H. L. and M. K. N acknowledge funding from the European Union Seventh Framework Program [FP7/2007–2013] under grant agreement no. 604032 of the MESO project, (FP7/2007–2013) ENERGY.2012.10.2.1; NANOMATCELL, grant agreement no. 308997.

Notes and references

1 X. Zhu, H. Su, R. A. Marcus and M. E. Michel-Beyerle, *J. Phys. Chem. Lett.*, 2014, **5**, 3061–3065.

2 M. M. Lee, J. Teuscher, T. Miyasaka, T. N. Murakami and H. J. Snaith, *Science*, 2012, **338**, 643–647.

3 J. Burschka, N. Pellet, S. J. Moon, R. Humphry-Baker, P. Gao, M. K. Nazeeruddin and M. Gratzel, *Nature*, 2013, **499**, 316–319.

4 T. C. Sum and N. Mathews, *Energy Environ. Sci.*, 2014, **7**, 2518–2534.

5 M. Gratzel, *Nat. Mater.*, 2014, **13**, 838–842.

6 H. J. Snaith, *J. Phys. Chem. Lett.*, 2013, **4**, 3623–3630.

7 Z.-K. Tan, R. S. Moghaddam, M. L. Lai, P. Docampo, R. Higler, F. Deschler, M. Price, A. Sadhanala, L. M. Pazos, D. Credgington, F. Hanusch, T. Bein, H. J. Snaith and R. H. Friend, *Nat. Nanotechnol.*, 2014, **9**, 687–692.

8 G. Xing, N. Mathews, S. S. Lim, N. Yantara, X. Liu, D. Sabba, M. Grätzel, S. Mhaisalkar and T. C. Sum, *Nat. Mater.*, 2014, **13**, 476–480.

9 X. Y. Chin, D. Cortecchia, J. Yin, A. Bruno and C. Soci, *Nat. Commun.*, 2015, **6**, 7383.

10 V. D'Innocenzo, G. Grancini, M. J. P. Alcocer, A. R. S. Kandada, S. D. Stranks, M. M. Lee, G. Lanzani, H. J. Snaith and A. Petrozza, *Nat. Commun.*, 2014, **5**, 1–6.

11 Q. Lin, A. Armin, R. C. R. Nagiri, P. L. Burn and P. Meredith, *Nat. Photonics*, 2015, **9**, 106–112.

12 C. Wehrenfennig, G. E. Eperon, M. B. Johnston, H. J. Snaith and L. M. Herz, *Adv. Mater.*, 2014, **26**, 1584–1589.

13 S. D. Stranks, G. E. Eperon, G. Grancini, C. Menelaou, M. J. P. Alcocer, T. Leijtens, L. M. Herz, A. Petrozza and H. J. Snaith, *Science*, 2013, **342**, 341–344.

14 E. T. Hoke, D. J. Slotcavage, E. R. Dohner, A. R. Bowring, H. I. Karunadasa and M. D. McGehee, *Chem. Sci.*, 2015, **6**, 613–617.

15 A. Kojima, K. Teshima, Y. Shirai and T. Miyasaka, *J. Am. Chem. Soc.*, 2009, **131**, 6050–6051.

16 http://www.nrel.gov/pv/.

17 A. Marchioro, J. Teuscher, D. Friedrich, M. Kunst, R. van de Krol, T. Moehl, M. Gratzel and J. E. Moser, *Nat. Photonics*, 2014, **8**, 250–255.

18 G. Grancini, A. R. Srimath Kandada, J. M. Frost, A. J. Barker, M. De Bastiani, M. Gandini, S. Marras, G. Lanzani, A. Walsh and A. Petrozza, *Nat. Photonics*, 2015, **9**, 695–701.

19 P. Piatkowski, B. Cohen, F. Javier Ramos, M. Di Nunzio, M. K. Nazeeruddin, M. Gratzel, S. Ahmad and A. Douhal, *Phys. Chem. Chem. Phys.*, 2015, **17**, 14674–14684.

20 E. Mosconi, A. Amat, M. K. Nazeeruddin, M. Grätzel and F. De Angelis, *J. Phys. Chem. C*, 2013, **117**, 13902–13913.

21 E. Mosconi, C. Quarti, T. Ivanovska, G. Ruani and F. De Angelis, *Phys. Chem. Chem. Phys.*, 2014, **16**, 16137–16144.

22 H.-S. Kim, C.-R. Lee, J.-H. Im, K.-B. Lee, T. Moehl, A. Marchioro, S.-J. Moon, R. Humphry-Baker, J.-H. Yum, J. E. Moser, M. Gratzel and N.-G. Park, *Sci. Rep.*, 2012, **2**, 591.

23 C. Liu, K. Wang, P. Du, T. Meng, X. Yu, S. Z. D. Cheng and X. Gong, *ACS Appl. Mater. Interfaces*, 2014, **7**, 1153–1159.

24 J. H. Heo, D. H. Song and S. H. Im, *Adv. Mater.*, 2014, **26**, 8179–8183.

25 J. Teuscher, A. Ulianov, O. Müntener, M. Grätzel and N. Tétreault, *ChemSusChem*, 2015, **8**, 3847–3852.

26 L. Etgar, P. Gao, Z. Xue, Q. Peng, A. K. Chandiran, B. Liu, M. K. Nazeeruddin and M. Grätzel, *J. Am. Chem. Soc.*, 2012, **134**, 17396–17399.

27 M. Saliba, T. Matsui, J.-Y. Seo, K. Domanski, J.-P. Correa-Baena, N. Mohammad K, S. M. Zakeeruddin, W. Tress, A. Abate, A. Hagfeldt and M. Gratzel, *Energy Environ. Sci.*, 2016, DOI: 10.1039/C5EE03874J.

28 J. H. Heo, S. H. Im, J. H. Noh, T. N. Mandal, C. S. Lim, J. A. Chang, Y. H. Lee, H. J. Kim, A. Sarkar, M. K. Nazeeruddin, M. Gratzel and S. I. Seok, *Nat. Photonics*, 2013, **7**, 487–492.

29 J. C. Brauer, Y. H. Lee, M. K. Nazeeruddin and N. Banerji, *J. Phys. Chem. Lett.*, 2015, **6**, 3675–3681.

30 C. S. Ponseca, E. M. Hutter, P. Piatkowski, B. Cohen, T. Pascher, A. Douhal, A. Yartsev, V. Sundstrom and T. J. Savenije, *J. Am. Chem. Soc.*, 2015, **137**, 16043–16048.

31 M. R. Filip, C. Verdi and F. Giustino, *J. Phys. Chem. C*, 2015, **119**, 25209–25219.

32 C. Motta, F. El-Mellouhi, S. Kais, N. Tabet, F. Alharbi and S. Sanvito, *Nat. Commun.*, 2015, **6**, 7026.

33 J. Even, *J. Phys. Chem. Lett.*, 2015, **6**, 2238–2242.

34 J. Even, L. Pedesseau and C. Katan, *J. Phys. Chem. C*, 2014, **118**, 11566–11572.

35 J. Even, L. Pedesseau, C. Katan, M. Kepenekian, J.-S. Lauret, D. Sapori and E. Deleporte, *J. Phys. Chem. C*, 2015, **119**, 10161–10177.

36 G. Xing, N. Mathews, S. Sun, S. S. Lim, Y. M. Lam, M. Grätzel, S. Mhaisalkar and T. C. Sum, *Science*, 2013, **342**, 344–347.

37 A. Marchioro, EPFL thesis, 2014, vol. 6221.

38 T. C. Sum, N. Mathews, G. Xing, S. S. Lim, W. K. Chong, D. Giovanni and H. A. Dewi, *Acc. Chem. Res.*, 2016, **49**, 294–302.

39 M. B. Price, J. Butkus, T. C. Jellicoe, A. Sadhanala, A. Briane, J. E. Halpert, K. Broch, J. M. Hodgkiss, R. H. Friend and F. Deschler, *Nat. Commun.*, 2015, **6**, 8420.

40 Y. Yang, D. P. Ostrowski, R. M. France, K. Zhu, J. van de Lagemaat, J. M. Luther and M. C. Beard, *Nat. Photonics*, 2016, **10**, 53–59.

41 K. G. Stamplecoskie, J. S. Manser and P. V. Kamat, *Energy Environ. Sci.*, 2015, **8**, 208–215.

42 O. Flender, J. R. Klein, T. Lenzer and K. Oum, *Phys. Chem. Chem. Phys.*, 2015, **17**, 19238–19246.

43 K. Chen, A. J. Barker, F. L. C. Morgan, J. E. Halpert and J. M. Hodgkiss, *J. Phys. Chem. Lett.*, 2015, **6**, 153–158.

44 C. S. Ponseca, T. J. Savenije, M. Abdellah, K. B. Zheng, A. Yartsev, T. Pascher, T. Harlang, P. Chabera, T. Pullerits, A. Stepanov, J. P. Wolf and V. Sundstrom, *J. Am. Chem. Soc.*, 2014, **136**, 5189–5192.

45 G. Xing, B. Wu, S. Chen, J. Chua, N. Yantara, S. Mhaisalkar, N. Mathews and T. C. Sum, *Small*, 2015, **11**, 3606–3613.

46 Y. X. Zhai, C. X. Sheng, C. Zhang and Z. V. Vardeny, *Adv. Funct. Mater.*, 2016, **26**, 1617–1627.

47 G. Grancini, S. Marras, M. Prato, C. Giannini, C. Quarti, F. De Angelis, M. De Bastiani, G. E. Eperon, H. J. Snaith,

L. Manna and A. Petrozza, *J. Phys. Chem. Lett.*, 2014, **5**, 3836–3842.
48 A. Miyata, A. Mitioglu, P. Plochocka, O. Portugall, J. T.-W. Wang, S. D. Stranks, H. J. Snaith and R. J. Nicholas, *Nat. Phys.*, 2015, **11**, 582–587.
49 E. Menéndez-Proupin, P. Palacios, P. Wahnón and J. C. Conesa, *Phys. Rev. B: Condens. Matter Mater. Phys.*, 2014, **90**, 045207.
50 H. P. Zhou, Q. Chen, G. Li, S. Luo, T. B. Song, H. S. Duan, Z. R. Hong, J. B. You, Y. S. Liu and Y. Yang, *Science*, 2014, **345**, 542–546.
51 D. Shi, V. Adinolfi, R. Comin, M. J. Yuan, E. Alarousu, A. Buin, Y. Chen, S. Hoogland, A. Rothenberger, K. Katsiev, Y. Losovyj, X. Zhang, P. A. Dowben, O. F. Mohammed, E. H. Sargent and O. M. Bakr, *Science*, 2015, **347**, 519–522.
52 H. S. Duan, H. P. Zhou, Q. Chen, P. Y. Sun, S. Luo, T. B. Song, B. Bob and Y. Yang, *Phys. Chem. Chem. Phys.*, 2015, **17**, 112–116.
53 M. Samiee, S. Konduri, B. Ganapathy, R. Kottokkaran, H. A. Abbas, A. Kitahara, P. Joshi, L. Zhang, M. Noack and V. Dalal, *Appl. Phys. Lett.*, 2014, **105**, 153502.
54 A. Baumann, S. Vath, P. Rieder, M. C. Heiber, K. Tvingstedt and V. Dyakonov, *J. Phys. Chem. Lett.*, 2015, **6**, 2350–2354.
55 D. W. deQuilettes, S. M. Vorpahl, S. D. Stranks, H. Nagaoka, G. E. Eperon, M. E. Ziffer, H. J. Snaith and D. S. Ginger, *Science*, 2015, **348**, 683–686.
56 W. H. Nguyen, C. D. Bailie, E. L. Unger and M. D. McGehee, *J. Am. Chem. Soc.*, 2014, **136**, 10996–11001.
57 U. Bach, EPFL thesis, 2000, vol. 2187.